Available online at www.sciencedirect.com
SCIENCE DIRECT®
Acta Materialia 53 (2005) 1883–1893
Acta MATERIALIA
www.actamat-journals.com

Micromechanics of deformation of metallic-glass–matrix composites from in situ synchrotron strain measurements and finite element modeling

R.T. Ott [a,*], F. Sansoz [b], J.F. Molinari [c], J. Almer [d], K.T. Ramesh [c], T.C. Hufnagel [a]

[a] Department of Materials Science and Engineering, Johns Hopkins University, Baltimore, MD 21218, USA
[b] Department of Mechanical Engineering, University of Vermont, Burlington, VT 05405, USA
[c] Department of Mechanical Engineering, Johns Hopkins University, Baltimore, MD 21218, USA
[d] Argonne National Laboratory, Advanced Photon Source, Argonne, IL 60439, USA

Received 29 November 2004; accepted 31 December 2004
Available online 29 January 2005

Abstract

We have used in situ X-ray scattering and finite element modeling (FEM) to examine the micromechanics of deformation of in situ formed metallic-glass–matrix composites consisting of Ta-rich particles dispersed in an amorphous matrix. The strain measurements show that under uniaxial compression the second-phase particles yield at an applied stress of ~325 MPa. After yielding, the particles do not strain harden significantly; we show that this is due to an increasingly hydrostatic stress state arising from the lateral constraint on deformation of the particles imposed by the elastic matrix. Shear band initiation in the matrix is not due to the difference in elastic properties between the matrix and the particles. Rather, the development of a plastic misfit strain causes stress concentrations around the particles, resulting in localized yielding of the matrix by shear band formation at an applied stress of ~1450 MPa, considerably lower than the macroscopic yield stress of the composite (~1725 MPa). Shear bands do not propagate at the lower stress because the yield criterion of the matrix is only satisfied in the region immediately around the particles. At the higher stresses, the yield criterion is satisfied in large regions of the matrix, allowing extensive shear band propagation and significant macroscopic plastic deformation. However, the presence of the particles makes the stress state highly inhomogeneous, which may partially explain why fracture is suppressed in the composite, allowing the development of large plastic strains.

Keywords: Metallic glass; Composites; X-ray diffraction; FEM; Micromechanics

1. Introduction

Metallic glasses combine some of the advantageous mechanical properties of metals, such as high strength, with the processing flexibility of glasses. This makes them attractive candidates for a variety of load-bearing applications. The lack of strain hardening, however, means that single-phase metallic glasses experience shear localization, which leads to fracture after only limited macroscopic plastic deformation. For this reason, considerable effort has been devoted to the development of two-phase materials consisting of crystalline particles in a metallic-glass–matrix [1–7]. These second-phase particles cause the plastic strain to be distributed over a larger volume of material, delaying the onset of fracture.

Both in situ composites, in which a crystalline phase is precipitated from the melt during cooling, and ex situ composites, in which the reinforcing phase is physically

* Corresponding author. Present address: Materials and Engineering Physics, Ames National Laboratory, 105 Metals development, Ames, IA 50011, USA. Tel.: +1 515 294 3616; fax: +1 515 294 8727.
E-mail address: rtott@ameslab.gov (R.T. Ott).

1359-6454/$30.00
doi:10.1016/j.actamat.2004.12.037

added to the metallic glass prior to casting, have been developed. In situ composites have the advantage of being able to produce a finer microstructure of the crystalline phase, but are quite sensitive to the processing conditions (particularly the cooling rate) and are specific to particular amorphous alloy compositions. Ex situ composites, on the other hand, can be produced from virtually any bulk amorphous alloy, but only a limited range of length scales of the microstructure are possible.

We have developed a hybrid process for making metallic-glass–matrix composites, in which a high-melting point crystalline phase is precipitated from a metastable crystalline solid solution in a separate step prior to casting of the composite [5,8]. When the alloy is heated to cast the composite, the crystalline phase does not melt, so the particles are retained in the final composite microstructure. By appropriate control of the precipitation process, we can achieve particle sizes in the composite ranging from 0.1 to 100 μm. Although to date, we have used this process to produce Ta-rich particles in Zr-based metallic glasses, in principle a similar process could be applied to any amorphous alloy in which one element shows a solid-state miscibility gap with a refractory metal such as Ta, W, or Nb.

Unlike conventional metal–matrix composites, the reinforcing phase in metallic-glass–matrix composites typically has a lower yield stress than the matrix. During loading, the particles experience plastic deformation, while the stronger glass matrix remains elastic. When the applied stress becomes sufficiently high, plastic deformation in the matrix occurs by the formation and propagation of shear bands. Since the initiation of shear bands depends on the load transfer between the second-phase particles and the matrix, understanding the details of this process is important for understanding the macroscopic mechanical behavior of the composites.

Recently, Balch and coworkers [9,10] used high energy X-ray scattering to measure the lattice strains in crystalline reinforcements in ex situ metallic-glass–matrix composites during both uniaxial compression and uniaxial tension. They examined the load transfer between the amorphous matrix and the second-phase particles during loading and unloading, and found that the crystalline particles yielded before the matrix, decreasing the fraction of the subsequent load transferred to particles. For composites with small (1–2 μm) Ta particles loaded in compression, they found that the Ta particles yielded at an applied stress of −800 MPa. This corresponds to a von Mises effective stress of 1500 MPa, much larger than that expected for yielding of pure Ta (~200 MPa). Balch and coworkers attributed the high yield stress of the particles to their small size and to possible solid-solution strengthening. For somewhat larger Ta particles (~9 μm) tested in tension, they observed yielding at a von Mises stress of 200 MPa, which is more consistent with the expected value for pure Ta. They also found that, for samples loaded in tension, the Ta particles yielded in compression during unloading due to the large elastic strain stored in the glass matrix.

In this paper, we examine the micromechanics of deformation of the in situ formed composite alloys under uniaxial compression using high-energy X-ray scattering and finite element modeling (FEM). We show that the particles yield at relatively low stresses. The plastic misfit strain plays a key role, limiting the ability of the particles to strain harden (due to an increasingly hydrostatic stress state from the matrix constraint) and ultimately inducing stress concentrations in the matrix that cause it to yield at applied stresses significantly lower than the macroscopic yield stress of the composite.

2. Experimental and numerical approach

2.1. Sample preparation

Composite alloys of composition $(Zr_{70}Cu_{20}Ni_{10})_{90-x}Ta_xAl_{10}$ (x = 6, 8, and 10 at.% Ta) were prepared by arc melting and suction casting. The process is described in detail elsewhere [5], but the basic steps are to prepare a metastable Zr–Ta binary ingot, followed by melting this ingot together with Cu, Ni, and Al to make a master alloy ingot for casting. During the second melting step, some of the Ta precipitates out to form ~10 μm particles. The alloys were suction cast into a copper mold to form rods 3.2 mm in diameter. For the synchrotron strain measurements, the samples were machined to cylindrical rods or rectangular prisms with an aspect ratio of 2:1. The ends of the samples were polished to ensure parallelism and the surfaces of all of the samples were mirror polished in order to minimize scattering from surface scratches.

A typical microstructure for these specimens is shown in Fig. 1(a). Some of the Ta particles agglomerate during casting into larger (~50–100 μm) clusters. The volume fraction of the Ta particles ranges from approximately 2% (for x = 6% Ta) to approximately 6% (for x = 10% Ta). The composition of the particles, as determined by electron microprobe analysis, is 93 at.% Ta, 6% Zr, and 1% Cu + Ni + Al.

2.2. Synchrotron strain measurements

We performed the in situ strain measurements at beamline 1-ID beamline of the Advanced Photon Source at Argonne National Laboratory. Using a screw-driven load cell, we loaded the samples incrementally in uniaxial compression from 0 to 1600–1800 MPa and unloaded back to 0 MPa external stress. The loading was stopped during the X-ray measurements. We used monochromatic 80.72 keV (0.0154 nm) X-rays with a square beam of 0.1×0.1 mm to measure the lattice strains for each

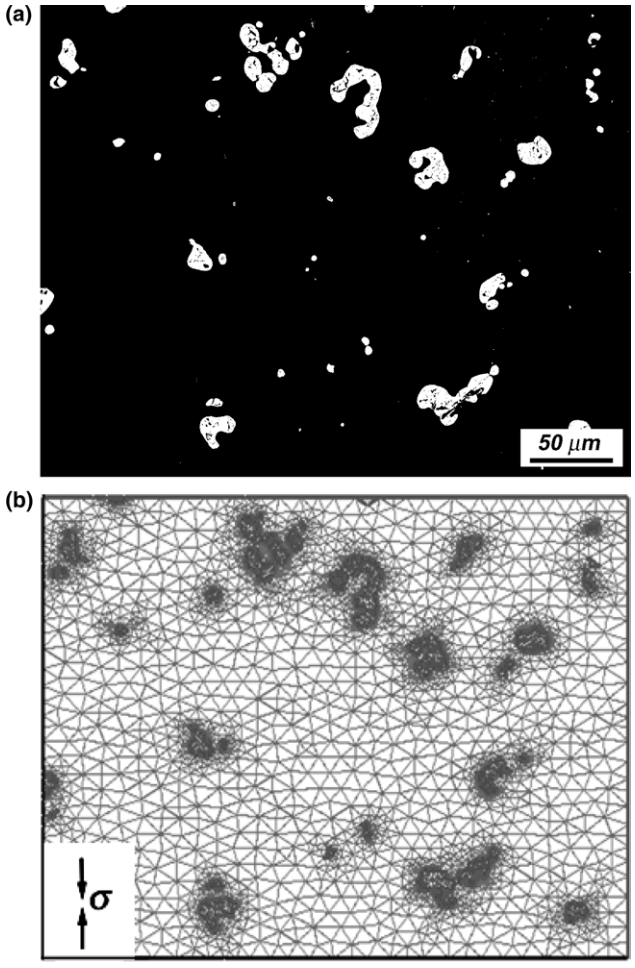

Fig. 1. (a) Backscattered SEM micrograph of 8% Ta containing alloy and (b) corresponding mesh used in FEM calculations.

load. A digital image plate (MAR 345) with a 150×150 μm pixel size was positioned 975 mm downstream from the sample to record the scattered intensity. A typical diffraction pattern recorded by the digital image plate is shown in Fig. 2. Because of the small volume fraction and large particle size, continuous powder rings are not observed; instead, we see discrete spots, each of which corresponds to diffraction by a single Ta domain.

As pointed out by Wanner and Dunand [11], the interplanar spacing of a family of crystallographic planes can be expressed as

$$d = \frac{\lambda}{2\sin\left(\frac{1}{2}\arctan\left(\frac{D}{2L}\right)\right)}, \tag{1}$$

where λ is the X-ray wavelength, D is the diameter of the powder rings on image plate, and L is the camera length (the distance between the sample and the image plate). From Eq. (1), the elastic strain in the Ta particles for a given externally applied stress can be calculated from

$$\varepsilon = \ln\left(\frac{d}{d_0}\right), \tag{2}$$

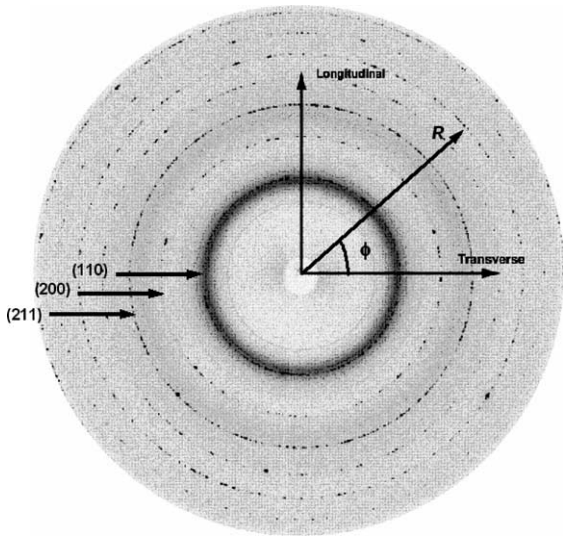

Fig. 2. Typical diffraction pattern on digital image plate. The longitudinal and transverse directions are denoted.

where ε is the lattice strain and d_0 is unstrained d-spacing.

Eqs. (1) and (2) assume that the camera length L and the X-ray wavelength λ are known and do not change during the course of the experiment. However, L can change if the sample surface is displaced during loading (due to a Poisson effect, for instance) and the X-ray wavelength can drift (although this effect is usually small). For some of our experiments, we accounted for these uncertainties by attaching an external standard (Ce_2O_3 powder) of known d-spacing to the surface of the sample and calculating the strain from

$$\varepsilon_s = \frac{d^s - d_0^s}{d_0^s} \approx 1 - \frac{D^s}{D_0^s}\frac{D_0^c}{D^c}, \tag{3}$$

where ε_s is the lattice strain, d_0 is the unstrained lattice spacing of the sample, d is the strained lattice spacing, D_0^s and D_0^c are the reference state diameters of the Debye rings for the sample and the calibration substance, respectively, and D^s and D^c are the strained diameters of the Debye rings for the sample and calibration substance, respectively [11]. For several samples, we used both methods (Eqs. (2) and (3)) for calculating the lattice strains. For the most part, the two methods yield similar results, and our conclusions below are not affected by whether or not a standard was used. However, the difference can become important for situations where there is a large plastic strain (resulting in a large displacement of the sample surface) but the elastic strain (which is the only strain component measured in X-ray scattering) is small.

One advantage of high-energy X-ray scattering is the ability to perform in situ transmission experiments on bulk samples. Since the X-ray wavelength is small, the crystallographic planes that satisfy the Bragg conditions

are nearly parallel to the incident beam; for the Ta (2 1 1) planes examined here, the Bragg angle (2θ) is 6.5°. Therefore, with a two-dimensional detector the lattice strain for the longitudinal (parallel to loading axis) and transverse (perpendicular to loading axis) directions can be simultaneously measured along with the strain for all angles ϕ. We assume that under uniaxial loading the strains in the two transverse directions are identical, allowing us to determine the full three-dimensional strain state of the sample.

For an unstrained sample (or one in a state of hydrostatic strain), the powder rings appear as circles on the digital image plate since the d-spacing is the same for all angles ϕ (assuming that the detector is orthogonal to the incident X-ray beam). When a uniaxial stress is applied to the sample, the rings are distorted into ellipses due to the dependence of the strain state on ϕ. The semi-axes of the ellipse can be taken as the longitudinal and transverse strain directions due to the small Bragg angle. In order to obtain reliable strain measurements, the semi-axes of the ellipses must be measured accurately. We accomplished this by using a data analysis procedure similar to that used by Wanner and Dunand [11], in which the diameter of the ring for all angles ϕ are plotted against $\sin^2\phi$. Plotted in this way, the data fall on a line; and a least-squares fit to the data allows determination of the semi-axes of the ellipse.

We chose the Ta {2 1 1} reflection for calculating the strain in the Ta particles since it is a strong peak and not significantly convoluted with the scattering "halo" from the amorphous matrix. For some specimens, we also examined the Ta {1 1 0} and {3 1 0} peaks and find no significant differences in the measured lattice strains. This allows us to assume that the particles behave in an elastically isotropic manner.

2.3. Finite element modeling

X-ray scattering only provides information on the strain state of the particles. To examine the strain state of the amorphous matrix, we built a two-dimensional plane-strain computational model using the FEM. To create a mesh that captures the morphology and dimensions of the microstructure, we used the mesh-generating program ppm2oof [12] together with scanning electron micrographs of the microstructure, as illustrated in Fig. 1.

We conducted the FEM calculations by assigning a series of compressive load increments in the top boundary of the mesh and constraining the bottom nodes in the direction of loading. A symmetry plane was enforced on the left side of the mesh by fixing the displacement of nodes in a direction perpendicular to the loading axis. The resolution scheme is based on a Lagrangian framework using an explicit time integration algorithm. Further details on the implementation of this method [13].

A small-deformation plasticity model with non-linear isotropic hardening was chosen to model the constitutive behavior of the Ta-rich particles. In this model, the closed-form of the strain hardening curve is related to the plastic strain, ε^{p}, by:

$$g(\varepsilon^{\mathrm{p}}) = \sigma_{\mathrm{y}}\left(1 + \frac{\varepsilon^{\mathrm{p}}}{\varepsilon_0^{\mathrm{p}}}\right)^{1/n}, \tag{4}$$

where $\varepsilon_0^{\mathrm{p}}$ is the reference plastic strain, ε^{p} is the plastic strain, n is the hardening exponent and σ_{y} is the yield stress at the onset of plastic deformation under uniaxial loading. In this expression, the plastic strain is given by [14]:

$$\varepsilon^{\mathrm{p}} = \sqrt{\frac{2}{3}} \times \int_0^t \sqrt{\dot{\varepsilon}_{ij}^{\mathrm{p}} \dot{\varepsilon}_{ij}^{\mathrm{p}}}\, \mathrm{d}t. \tag{5}$$

Rate hardening effects are small under quasi-static loading and therefore are neglected.

The elastic properties and constitutive model parameters for the two phases used as input to the finite element model are listed in Table 1. We assume that the constitutive behavior of the Zr-based amorphous matrix is elastic-perfectly plastic with a yield stress corresponding to the maximum stress before failure of the single-phase glass. Since we cannot make single-phase amorphous alloys of the same composition as the matrix without precipitating out some Ta particles, we assumed a yield stress of 1750 MPa. This is consistent with the reported yield stress for amorphous alloys of similar composition [15,16].

The properties of the Ta particles are more problematic, due to the significant level of Zr in solid solution and the effect of the grain size. We have tested Ta-rich alloys of similar composition to the particles (Ta–7% Zr) in uniaxial compression and find that the yield stress is 335 ± 50 MPa, compared to 120 MPa for pure Ta [17]. For the FEM model, we used a yield stress of 350 MPa, which is consistent with our measurement and which gives reasonable agreement with the scattering data (as shown below). To model the strain hardening behavior, we used power-law parameters for pure Ta [17,18]. However, the particles are not pure Ta, so this choice

Table 1
Constitutive properties of Ta particles and glass matrix for FEM calculations

Material	σ_{y} (MPa)	E (GPa)	ν	$\varepsilon_0^{\mathrm{p}}$	N
Ta particles	350	185 [22]	0.34 [22]	0.00556 [18]	0.61 [17]
Zr-based glass matrix	1750	85 [2]	0.38 [2]	–	–

may not accurately capture the strain hardening behavior, as we discuss in more detail below. In the FEM results presented below, we only consider the average value of each component of the stress tensor over all the elements constituting the Ta particles. The von Mises effective stress for the Ta particles was calculated on the basis of the average values of the stress. To account for any dynamical effects that might occur in the mesh during unloading, an appropriate amount of numerical viscosity was added.

3. Results and discussion

3.1. Thermal residual strains

A difference in coefficients of thermal expansion between the matrix and the particles causes residual strains to develop during cooling. The magnitude of these strains can be calculated using the Eshelby equivalent inclusion method [19,20]. We assume that any stresses that might develop above the glass transition temperature (673 K) can be accommodated by viscous flow in the supercooled liquid, and that no plastic flow occurs below the glass transition. We calculate the thermal strains in the Ta particles for the 6%, 8%, and 10% Ta alloys to be −141, −139, and −133 με, respectively, and the corresponding residual stresses to be −76, −75, and −72 MPa, respectively. (We use "με" to refer to a strain of 1×10^{-6}.) Under the assumption that the Ta particles are essentially spherical, the thermal residual strain is hydrostatic. In the data presented below, this thermal strain is simply added to the measured strains of the particles in the composites. The thermal residual stress in the glassy matrix is less than 10 MPa (tensile) for all the alloys and we neglect it in what follows.

3.2. Deformation of Ta particles during loading

The applied stress vs. lattice strain for the Ta particles measured from the bcc-Ta 2 1 1 peak during a loading–unloading cycle is shown in Fig. 3. The strains in the longitudinal (parallel to the loading axis) and transverse (perpendicular to the loading axis) directions are shown along with the predicted elastic strain calculated using the Eshelby equivalent inclusion method [20].

For applied stresses below 325 MPa (compressive), the measured lattice strains in both directions are linear, indicating elastic loading of the particles. At approximately 325 MPa applied stress, the particles yield, which causes increased load transfer to the amorphous matrix and a corresponding decrease in the fraction of load transferred to the particles. The glass matrix remains elastic since it has a much higher yield strength (∼1750 MPa) than the Ta particles (∼350 MPa). This

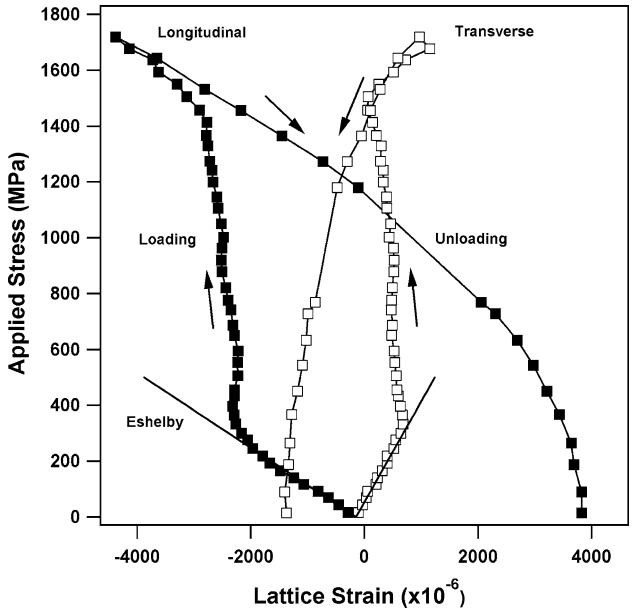

Fig. 3. Measured {2 1 1} lattice strain for Ta particles during uniaxial compression. The predicted elastic strain using the Eshelby equivalent inclusion method is also shown. Loading and unloading is indicated by the upward and downward arrows, respectively.

creates a plastic mismatch strain between the particles and the matrix, resulting in a stress that we refer to as the plastic misfit stress. The plastic misfit stress increases the load transfer to the matrix. At an applied stress of ∼1450 MPa, the lattice stress–strain curve changes slope again for both the longitudinal and transverse directions, indicating an increase in the fraction of the load being transferred to the Ta particles. This increase in load transfer to the particles is caused by yielding in the glass matrix and is discussed in more detail below.

Yielding in polycrystalline metals can be described using the von Mises criterion, so to further examine yielding of the particles, we calculated the von Mises effective stress from the measured strains. In the lattice strain measurements, the principal strains ε_2 (parallel to loading axis) and $\varepsilon_1 = \varepsilon_3$ (perpendicular to loading axis) correspond to the measured longitudinal and transverse strains, respectively. From the measured principal strains, the principal stresses in the particles can be calculated from [21]:

$$\sigma_1 = \sigma_3 = \frac{E}{1+v}\varepsilon_1 + \frac{vE}{(1+v)(1-2v)}(\varepsilon_1 + \varepsilon_2 + \varepsilon_3), \quad (6a)$$

$$\sigma_2 = \frac{E}{1+v}\varepsilon_2 + \frac{vE}{(1+v)(1-2v)}(\varepsilon_1 + \varepsilon_2 + \varepsilon_3), \quad (6b)$$

where σ_2 is the principal stress in the longitudinal direction and σ_1 and σ_3 are the principal stresses in the transverse directions. Eqs. (6a) and (6b) are based on isotropic elasticity; this is a reasonable approximation for Ta, and, as described above, the lattice strains are independent of the reflection chosen to calculate them.

From the principal stresses, the von Mises effective stress, σ_{eff}, can be calculated by

$$\sigma_{\text{eff}} = \frac{1}{\sqrt{2}}\left[(\sigma_1-\sigma_2)^2+(\sigma_2-\sigma_3)^2+(\sigma_3-\sigma_1)^2\right]^{1/2}. \quad (7)$$

Fig. 4 shows the von Mises effective stress of the Ta particles vs. the applied stress for an 8% Ta alloy loaded in uniaxial compression, calculated from the lattice strains shown in Fig. 3. For applied stresses below 325 MPa, the von Mises stress increases linearly, which is consistent with elastic loading in the particles. At an applied stress of ~325 MPa (which corresponds to a von Mises stress of 400 MPa), the von Mises stress exhibits a change in its slope indicating that the Ta particles have yielded. Following yielding, the von Mises stress remains relatively constant indicating an absence of work hardening. For applied stresses greater than 1450 MPa, the von Mises stress increases with increasing applied stress as the surrounding glass matrix yields.

The apparent lack of work hardening exhibited by the particles can be attributed to the plastic misfit strain that develops between the particles and the matrix. After yielding, under an assumption of constant-volume plastic deformation the effective Poisson's ratio of the particles becomes approximately 0.5. In contrast, the glass matrix, which remains elastic, has a Poisson's ratio of 0.38. As a result of this difference, the particles are constrained from expanding in the transverse directions.

The constraint of the particles by the matrix leads to the development of compressive stresses in the transverse directions. Fig. 5 shows the measured principal stresses in the longitudinal direction (σ_2) and the transverse directions (σ_1 and σ_3) obtained using Eqs. (6a) and (6b) and which were used to calculate the von Mises effective stress shown in Fig. 4. For applied stresses below 325 MPa (elastic loading of particles), the compressive stress in the longitudinal direction increases linearly while the transverse stresses remain nearly constant. After the particles yield, the stresses in the transverse directions become increasingly compressive due to the constraining effect of the matrix on the particles. Fig. 5(a) shows that the differences between the principal stresses (e.g., $\sigma_2-\sigma_1$) remain nearly constant with increasing applied stress (up to ~1450 MPa). Therefore, the von Mises stress of the particles remains unchanged over this range.

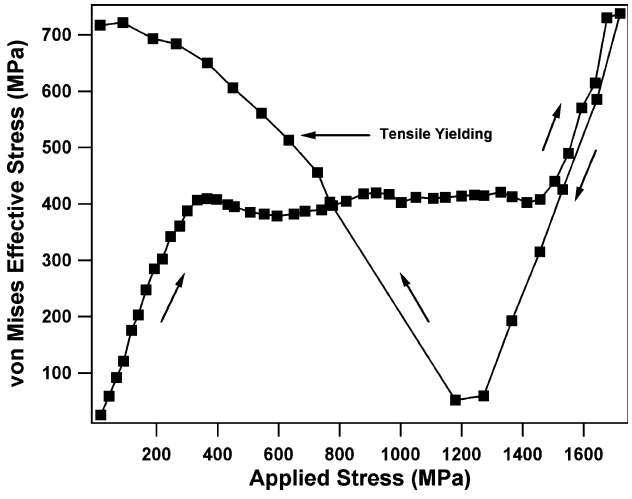

Fig. 4. von Mises effective stress vs. applied stress for a loading–unloading cycle of an 8% Ta alloy.

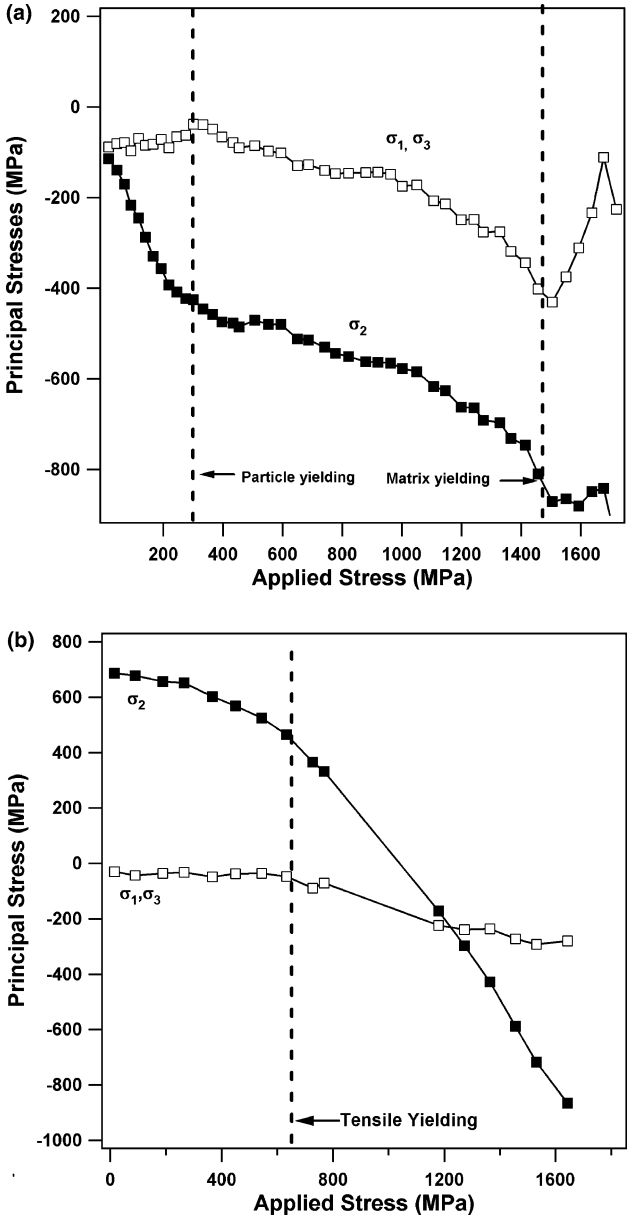

Fig. 5. Principal stresses as a function of applied stress for an 8% Ta alloy (a) during loading and (b) unloading in uniaxial compression. The principal stress σ_2 is along the loading axis and the σ_1 and σ_3 are perpendicular to the loading axis. Yielding in the particles and the glass matrix is marked by the dashed lines in (a) and tensile yielding is marked in (b).

For applied compressive stresses greater than 1450 MPa, both the von Mises stress (Fig. 4) and the principal stresses (Fig. 5(a)) exhibit a change in slope. In particular, the transverse stresses become less compressive. We attribute this to yielding in the matrix, which effectively removes the lateral constraint on the particles. Thus, once the matrix has yielded, the von Mises stress in the particles can increase and the particles can strain harden.

3.3. Deformation of Ta particles during unloading

Upon unloading, the compressive elastic strains in the Ta particles (Figs. 3 and 5(b)) and the corresponding von Mises stress (Fig. 4) relax. The strains become quite small and the von Mises stress nearly zero when the applied compressive stress reaches 1175 MPa, but at this stress, the amorphous matrix still has considerable stored elastic strain energy. Thus, further reductions in the applied stress cause a reversal of the strain state of the particles, into tension. As Fig. 3 shows, the tensile strain in the particles is elastic down to an applied stress of approximately 800 MPa, at which point the unloading curve deviates from linearity. This indicates tensile yielding of the particles at a von Mises stress of 500–600 MPa, somewhat lower than the maximum flow stress in compression (~700 MPa). Ordinarily for such a load reversal (compression followed by tension) one would expect that the flow stress in compression would become the yield stress in tension. The relatively low value of the yield stress in tension suggests that some other factor is in play. It may be that the relatively large hydrostatic tension stress affects the yield stress in tension. In any event, when the applied stress is completely removed, the Ta particles are left with a large residual tensile strain (~3800 με) in the longitudinal direction.

3.4. Cyclic loading/unloading

The residual strains that develop in the Ta particles after unloading can be seen more clearly by examining the lattice strain for a specimen subjected to several loading–unloading cycles. Fig. 6 shows the measured lattice strain of the Ta particles in the longitudinal direction for a 10% Ta alloy during four loading–unloading cycles; the corresponding von Mises stresses are shown in Fig. 7. The residual strain in the particles after unloading is dependent on the maximum applied stress during compressive loading. For the first loading cycle, the particles yield at an applied compressive stress of ~300 MPa, and there is little or no strain hardening apparent up to the maximum applied compressive stress of 500 MPa. When the specimen is unloaded, the elastic compressive strain is released and a small elastic tensile residual strain builds up in the particles; the corresponding residual von Mises stress is approximately 150 MPa.

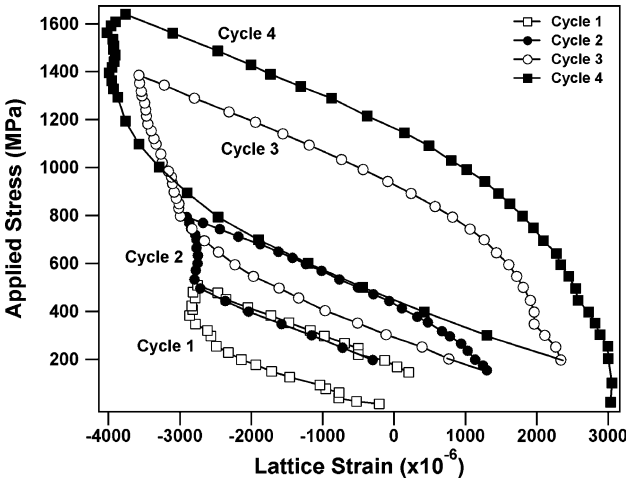

Fig. 6. Lattice strain in transverse direction for a 10% Ta alloy that has been subjected to four loading–unloading cycles.

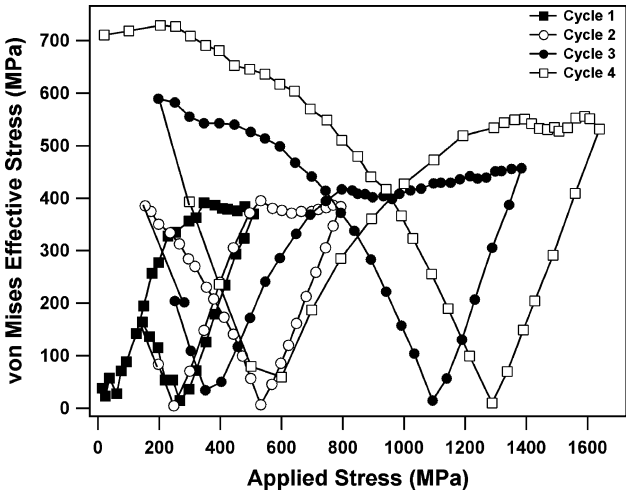

Fig. 7. von Mises effective stress vs. applied stress for a 10% Ta alloy that has undergone four loading–unloading cycles.

Since the particles did not yield in tension during the first cycle, upon reloading there is no hysteresis and the loading curve for the second cycle initially follows the unloading curve from the first cycle. The applied stress at which the particles yield in compression during the second cycle is higher than that of the first cycle, but the corresponding von Mises stresses at the yield points are approximately the same. The larger applied stress necessary for compressive yielding in the second loading cycle is due to the residual tensile stress that is present in the particles after unloading in the first cycle, which must be overcome by the applied compressive stress. For the second loading cycle, the maximum applied stress is ~800 MPa, which causes the particles to yield in tension during unloading and creates a larger residual tensile strain compared to the first unloading cycle.

Because the particles yield in tension during the second unloading, the loading path for the third cycle does

not coincide with the unloading path from the second cycle. The strain hardening due to tensile yielding affects the plastic deformation of the particles when they are reloaded in compression. The von Mises stress at yield is approximately constant (at 300–400 MPa), although not enough data points were collected to determine this conclusively. The flow stress, however, is significantly larger for the later cycles. For the last two loading–unloading cycles, the maximum applied stresses are increased, which increases the magnitude of the residual tensile strain. The hysteresis between the loading and unloading curves increases as the maximum applied stress increases.

3.5. Finite element modeling and shear band initiation

Fig. 8 shows the von Mises effective stress calculated using FEM along with experimental results for an 8% Ta alloy. In the elastic region, the agreement is good. The von Mises stress at which the particles yield, however, is lower for the FEM calculations (~300 MPa) than that observed experimentally (~350 MPa). It is likely that the discrepancy is due to the constitutive parameters used for the model (Table 1), which, as described above, are subject to some uncertainty. The discrepancy might also be due to the two-dimensional nature of the FEM model. The plane strain model changes the constraint on the particles, and, in particular, changes the transverse stress in the out-of-plane direction.

After the particles yield, FEM results indicate greater strain hardening than that which we observe experimentally. This discrepancy has two possible origins. The first relates to the plane-strain nature of the model. For the experimental results, the transverse principal stresses are assumed to be equal to each other since the particles are essentially equiaxial. In the FEM model, the transverse stresses are not equal to each other. As a result, the stress state predicted by FEM is less hydrostatic after particle yielding. This leads to greater work hardening than is experimentally observed. A second possibility is that the strain-hardening behavior assumed (from data for pure Ta) is inappropriate for these particles, which have significant alloy content.

At an applied compressive stress of 1450 MPa, the von Mises stress for the FEM calculations and the strain measurements both show a change in slope. As described above, we attribute this change in slope to yielding in the glass matrix. Interestingly, however, this yielding occurs at an applied stress that is significantly lower than 0.2% offset yield stress of the composite alloys, which is 1700 MPa (Fig. 9).

To better understand yielding of the matrix and the composite, recall from above that plastic deformation of Ta particles while the amorphous matrix is still elastic leads to the development of a plastic misfit strain in both phases. This misfit strain creates a significant stress concentration around the particles. Fig. 10 shows von Mises effective stress calculated using FEM for a single spherical Ta particle embedded in an amorphous matrix. (This simple system was chosen to eliminate the effects of shape anisotropy and the stress fields from other particles.) Even at applied stresses several hundred MPa below the yield stress of the matrix, the presence of the plastically deforming particle creates local stress concentrations that exceed the von Mises yield stress of the matrix. Note that although we have chosen a von Mises criterion for the matrix for convenience, we reach the same conclusion if we apply other yield criteria, such as Mohr–Coulomb.

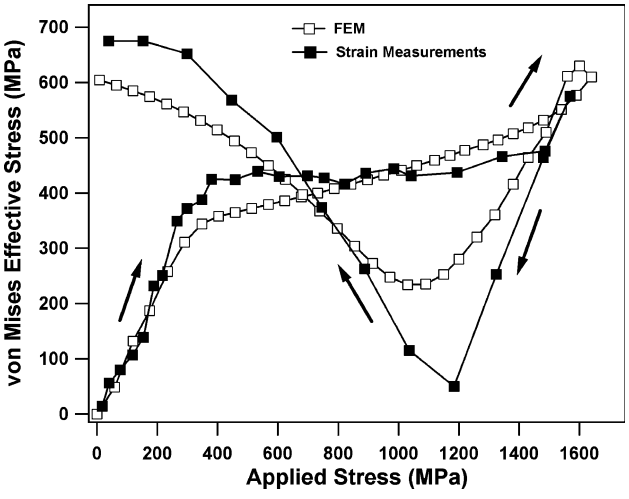

Fig. 8. von Mises effective stress as a function of applied stress calculated from synchrotron strain measurements (solid squares) and FEM (hollow squares). The arrows indicate the loading and unloading directions.

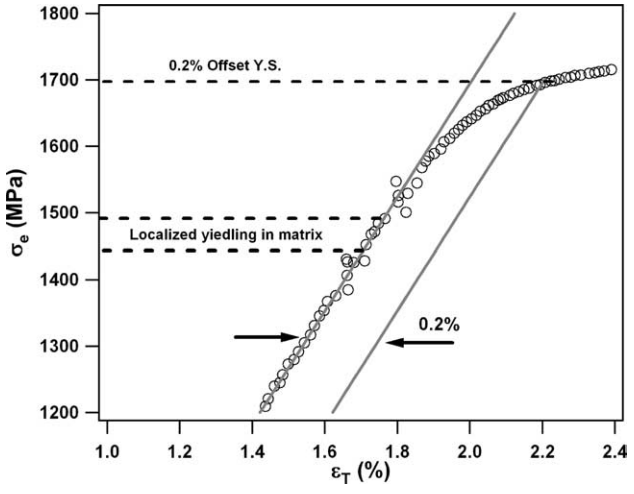

Fig. 9. Stress–strain curve for an 8% Ta alloy loaded in uniaxial compression. The strain was measured using a strain gauge attached to the sample. The 0.2% offset yield stress is noted along with the region where localized yielding occurs in the glass matrix.

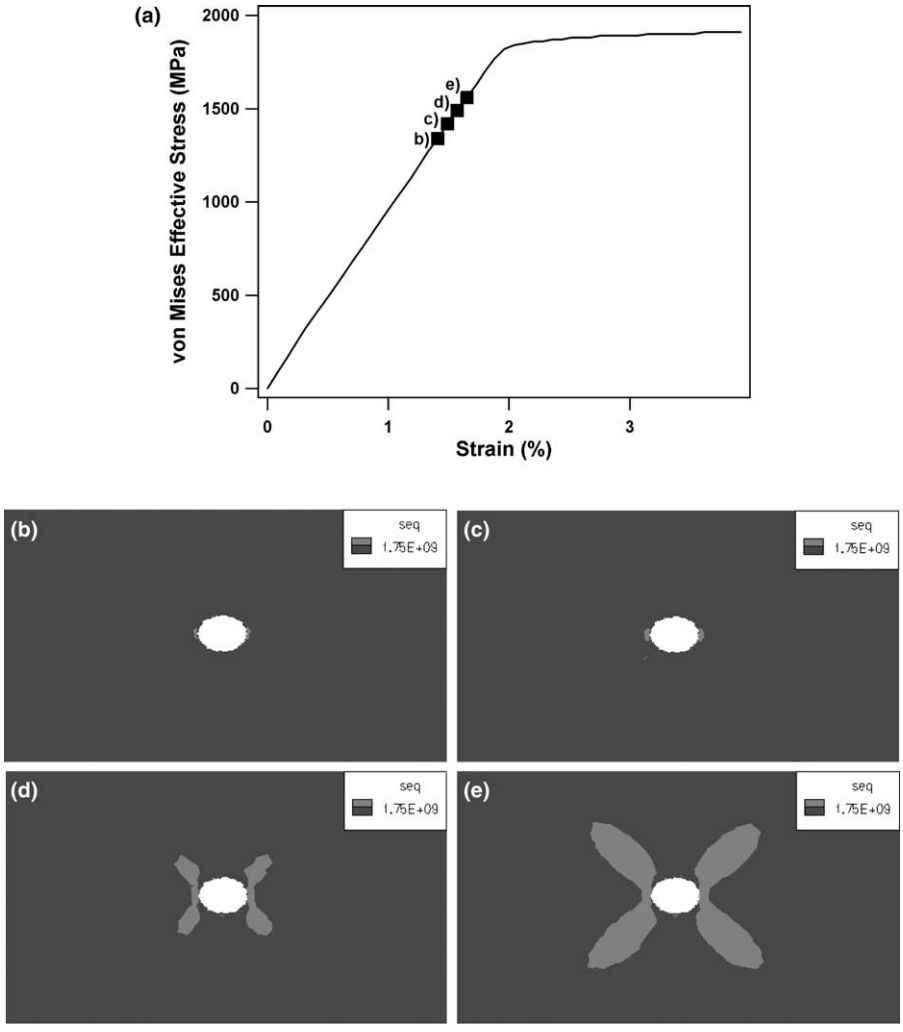

Fig. 10. Contour maps of von Mises effective stress for a single particle (white) embedded in an amorphous matrix. The images show the results for successive displacement steps increasing from (b) through (e). The light colored areas correspond to regions in the matrix where the von Mises stress is greater than 1750 MPa (the matrix yield stress). The corresponding stress for the contour maps is noted on the stress–strain curve (a).

Single-phase metallic glasses show behavior that is essentially elastic-perfectly plastic; that is, the yield stress and the flow stress are the same, because shear bands, once initiated, can propagate unhindered through the material. In the case of the composite materials, yielding of the matrix begins at ~1450 MPa, but this apparently does not initiate large-scale yielding of the composite. The FEM results in Fig. 10 suggest a possible explanation. At applied stresses below the yield stress of the matrix, the matrix yield criterion is only satisfied in the regions immediately around the particles. Thus, if a shear band initiates at the particle and propagates away, it will quickly encounter a region where the yield criterion is not satisfied and the shear stress is insufficient to sustain shear band propagation. This situation is exacerbated for systems of multiple particles, in which the stress state is highly inhomogeneous and there can even be regions where the von Mises stress is lower than the applied stress (Fig. 11). In addition to

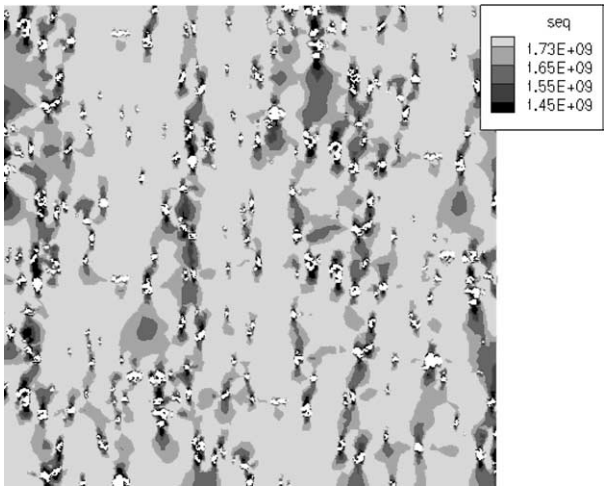

Fig. 11. Contour map of von Mises effective stress for an 8% Ta alloy. Note that the von Mises stress in certain regions of the matrix around the particles is much lower than the average matrix stress.

reducing the driving force for shear band propagation, under these conditions the plane of maximum shear stress can deviate locally from 45°, creating an opportunity for shear bands to be deflected. We expect that it is more difficult for shear bands to propagate under these conditions, and that this may explain why the composites can exhibit significant plastic strains prior to failure.

It is sometimes assumed for metallic-glass–matrix composites that it is a mismatch in the elastic properties of the matrix and reinforcement that causes shear band initiation. In the present case, however, where the yield stress of the particles is much lower than that of the matrix, this elastic misfit strain never creates a stress concentration in the amorphous matrix large enough to cause shear band initiation. Rather, it is the misfit strain that develops as a result of plastic deformation of the particles that is the primary source of stress concentration in the matrix. This observation suggests that the localized yielding in the glass matrix should be dependent on the yield stress of the Ta particles. If the yield stress of the particles is increased, then the applied stress at which the plastic misfit stress becomes sufficiently large to cause yielding in the matrix will also be increased. We have examined this effect with FEM. Fig. 12 shows the calculated von Mises effective stress for particles with different yield strengths as a function of applied stress for an 8% Ta alloy. Notice that the stress level at which a change in slope of the von Mises curves, indicative of yielding of the matrix, increases with increasing particle strength. This highlights the importance of yielding of the Ta particles on the developments of stress concentrations in the glass matrix. The initiation of shear bands in the matrix is dependent on the plastic misfit stress rather than the elastic mismatch between the phases.

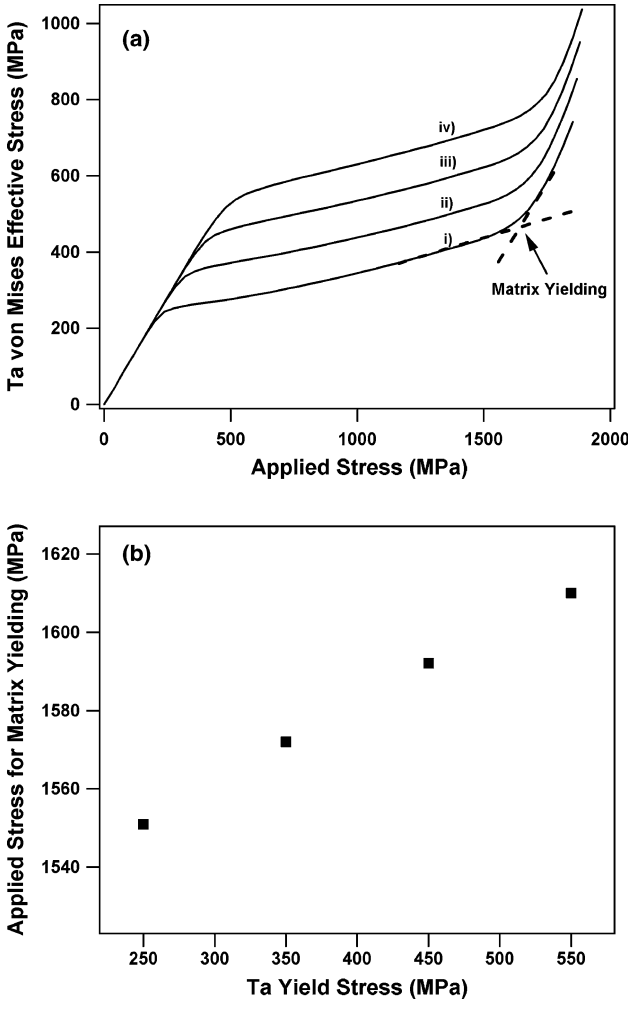

Fig. 12. (a) Calculated von Mises effective stress in the Ta particles vs. applied stress for an 8% Ta alloy. The yield strength of the particles was assumed to be (i) 250 MPa, (ii) 350 MPa, (iii) 450 MPa, and (iv) 550 MPa in the FEM calculations. (b) The applied stress at which localized yielding occurs in the glass matrix vs. the yield stress of the Ta particles.

While we cannot readily vary the yield stress of the second-phase particles in the composites in the as-cast state, the particles can be work hardened by subjecting the composite to a loading–unloading cycle such as that shown in Fig. 7. If the composite is loaded in compression to a stress significantly higher than the yield stress of the second-phase particles but lower than the yield stress of the matrix, upon unloading the particles will yield in tension and work harden This will increases the yield stress of the particles thus increase the applied stress at which shear bands initiate in the matrix. Whether this effect translates into an increased macroscopic yield stress of the composite would be an interesting direction for future investigations.

4. Conclusions

We have examined the micromechanics of deformation of in situ formed metallic-glass–matrix composites using synchrotron X-ray scattering and finite element modeling. For compressive loading, the particles yield at an applied stress of ~325 MPa, while the glass matrix remains elastic. After yielding, the particles experience little work hardening due to an increasingly hydrostatic stress state arising from the plastic misfit strain with the matrix. The misfit strain also creates stress concentrations in the matrix, leading to the initiation of shear bands at an applied stress significantly lower than the macroscopic yield stress of the composite alloys. Unloading of the composite causes the particles to yield in tension, causing strain hardening, increasing the flow stress of the particles upon subsequent reloading and possibly increasing the yield stress of the composite.

For the matrix, modeling results indicate that shear band initiation is not due to a mismatch in elastic properties with the particles. Rather, yielding occurs

due to the development of stress concentrations resulting from the plastic misfit strain. At an applied stress of ~1425 MPa, the yield criterion of the matrix is satisfied near the particles, leading to localized yielding by shear banding. At higher stresses approaching the macroscopic yield stress of the composite (~1725 MPa), the yield criterion is satisfied in larger regions of the matrix, allowing for macroscopic yielding. The presence of the particles creates a highly inhomogeneous stress distribution in the matrix, which may hinder shear band propagation and delay the onset of failure. Finally, we have found that the yield stress of the particles can be effectively increased by subjecting the composite to multiple loading cycles, which might provide a means to increase the yield stress of the composite alloys.

Acknowledgments

We gratefully acknowledge the assistance of David Dunand and Marcus Young with the in situ strain measurements, Derek Warner with the finite element modeling, and useful discussions with C.F., R.T.O., and T.C.H. acknowledge support for the in situ strain measurements from the US Department of Energy under Grant DE-FG02-98ER45699. Use of the Advanced Photon Source was supported by the US Department of Energy, Basic Energy Sciences, Office of Energy Research, under Contract No. W-31-109-Eng-38. Support for the finite element modeling was provided by the Center for Advanced Metallic and Ceramic Systems (CAMCS) at Johns Hopkins University, sponsored by the Army Research Laboratory (ARMAC-RTP) and accomplished under ARMAC-RTP Cooperative Agreement No. DAAD19-01-2-0003.

References

[1] Choi-Yim H, Busch R, Koster U, Johnson WL. Acta Mater 1999;47:2455.
[2] Choi-Yim H, Conner RD, Szuecs F, Johnson WL. Acta Mater 2002;50:2737.
[3] Hays CC, Kim CP, Johnson WL. Phys Rev Lett 2000;84:2901.
[4] Kuhn U, Eckert J, Mattern N, Schultz L. Appl Phys Lett 2002;80(14):2478.
[5] Fan C, Ott RT, Hufnagel TC. Appl Phys Lett 2002;81:1020.
[6] Hu X, Ng SC, Feng YP, Li Y. Acta Mater 2003;51:561.
[7] Ma H, Hu J, Ma E. Appl Phys Lett 2003;83:1020.
[8] Ott RT, Fan C, Li J, Hufnagel TC. J Non-Cryst Solids 2003;317:158.
[9] Balch DK, Ustundag E, Dunand DC. J Non-Cryst Solids 2003;317:176.
[10] Balch DK, Ustundag E, Dunand DC. Metall Mater Trans A 2003;34A:1787.
[11] Wanner A, Dunand DC. Metall Mater Trans A 2000;31A:2949.
[12] ppm2oof, software, http://www.ctcms.nist.gov/oof.
[13] Warner DH, Sansoz F, Molinari JF. Int. J. Plast. [submitted].
[14] Lemaitre J, Chaboche JL. Mechanics of solid materials. Cambridge: Cambridge University Press; 1990.
[15] Choi-Yim H, Schroers J, Johnson WL. Appl Phys Lett 2002;80:1906.
[16] Gu X. PhD Thesis. Johns Hopkins University; 2003.
[17] Khan AS, Liang R. Int J Plast 1999;15:1089.
[18] Chen SR, Gray III GT. Metall Mater Trans A 1996;27A:2994.
[19] Eshelby JD. Proc Roy Soc 1957;A241:376.
[20] Clyne TW, Withers PJ. An introduction to metal matrix composites. Cambridge: Cambridge University Press; 1993.
[21] Dieter G. Mechanical metallurgy. 3rd ed. Boston: McGraw-Hill; 1986.
[22] Handbook of elastic properties of solids, liquids, and gases. San Diego: Academic Press; 2001.